Atmos. Meas. Tech. Discuss., 6, 5621–5652, 2013
www.atmos-meas-tech-discuss.net/6/5621/2013/
doi:10.5194/amtd-6-5621-2013

Atmospheric Measurement Techniques Discussions
Open Access

Improvements to the OMI near UV aerosol algorithm using A-train CALIOP and AIRS observations

O. Torres[1], **C. Ahn**[2], **and Z. Chen**[2]

[1]NASA Goddard Space Flight Center, Greenbelt, Maryland, 20771, USA
[2]Science Systems and Applications, Inc., Lanham, Maryland, 20706, USA

Received: 19 April 2013 – Accepted: 5 June 2013 – Published: 21 June 2013

Correspondence to: O. Torres (omar.torres-2@nasa.gov)

Published by Copernicus Publications on behalf of the European Geosciences Union.

Abstract

The height of desert dust and carbonaceous aerosols layers and, to a lesser extent, the difficulty in determining the predominant size mode of these absorbing aerosol types, are sources of uncertainty in the retrieval of aerosol properties from near UV satellite observations. The availability of independent, near-simultaneous measurements of aerosol layer height, and aerosol-type related parameters derived from observations by other A-train sensors, makes possible the use of this information as input to the OMI (Ozone Monitoring Instrument) near UV aerosol retrieval algorithm (OMAERUV). A monthly climatology of aerosol layer height derived from observations by the CALIOP (Cloud–Aerosol Lidar with Orthogonal Polarization) sensor, and real-time AIRS (Atmospheric Infrared Sounder) CO observations are used in an upgraded version of the OMAERUV algorithm. AIRS CO measurements are used as a reliable tracer of carbonaceous aerosols, which allows the identification of smoke layers in regions and seasons when the dust-smoke differentiation is difficult in the near-UV. The use of CO measurements also enables the identification of elevated levels of boundary layer pollution undetectable by near UV observations alone. In this paper we discuss the combined use of OMI, CALIOP and AIRS observations for the characterization of aerosol properties, and show an improvement in OMI aerosol retrieval capabilities.

1 Introduction

Since the discovery of the near-UV capability of absorbing aerosols detection from space over a decade ago (Hsu et al., 1996; Herman et al., 1997; Torres et al., 1998), the UV Aerosol Index (AI), calculated from observations by the Total Ozone Mapping Spectrometer (TOMS) family of sensors, and more recently by the Ozone Monitoring Instrument (OMI), has been used to map the daily global distribution of UV-absorbing aerosols such as desert dust particles as well as carbonaceous aerosols generated by anthropogenic biomass burning and wild fires (Herman et al., 1997), and volcanic ash

AMTD
6, 5621–5652, 2013

injected in the atmosphere by volcanic eruptions (Seftor et al., 1999). The AI concept for aerosol detection has also been applied to other near-UV capable sensors such as GOME (Gleason et al., 1998; De Graaf et al., 2005a), and SCIAMACHY (de Vries et al., 2009; De Graaf et al., 2005b).

In addition to the qualitative AI product, near-UV retrieval algorithms of aerosol extinction optical depth (AOD) and single scattering albedo (SSA) making use satellite measurement in the 330–388 nm range have been applied to the TOMS (Torres et al., 1998, 2002) and OMI (Torres et al., 2007; Ahn et al. 2008) observations. The quantitative interpretation of the near-UV measurements in terms of aerosol absorption, however, is affected by the dependency of the measured radiances on the height of the absorbing aerosol layer (Torres et al., 1998; De Graaf et al., 2005a), and the difficulty in differentiating between carbonaceous and desert dust aerosol types especially over land.

In the absence of direct observations to diagnose the location of the aerosol layer in the atmosphere the TOMS aerosol algorithm (Torres et al., 2002) used a transport-model-generated climatology of aerosol layer height (Ginoux et al. 2001). To differentiate between absorbing aerosol types, the TOMS algorithm used geographical location and surface type considerations to prescribe the most likely absorbing aerosol type (carbonaceous or desert dust) present in the atmospheric column.

The near-simultaneity of satellite observations by a plurality of A-train sensors, provides the unprecedented opportunity of combining time and space collocated radiance observations and/or derived atmospheric parameters for global climate analysis (Anderson et al., 2005). Combined A-train measurements can also be used in inversion algorithms to further constrain retrieval conditions, and thus reduce the need of assumptions. CALIOP (Cloud–Aerosol Lidar with Orthogonal Polarization) measurements of the vertical distribution of the atmospheric aerosol load, and Atmospheric Infrared Sounder (AIRS) carbon monoxide (a reliable tracer of carbonaceous aerosols) observations, provide information that can be used to prescribe aerosol layer height and determine aerosol type in the OMI near UV aerosol algorithm (OMAERUV).

AMTD
6, 5621–5652, 2013

In this paper we discuss the use of observations by A-train sensors CALIOP and AIRS, to provide reliable information on aerosol layer height and aerosol type as input to OMAERUV. In Sect. 2, we briefly describe an improved version of the OMAERUV algorithm that utilizes CALIOP and AIRS observations as ancillary information. A detailed description of the way AIRS CO data is used in the OMI aerosol inversion procedure is presented in Sect. 3, followed by a discussion of the development of a CALIOP-based aerosol layer height climatology in Sect. 4, and an evaluation of the improved accuracy of OMI retrievals using AERONET observations in Sect. 5. Summary and final remarks are presented in Sect. 6.

2 The OMAERUV algorithm

OMI is a spectrograph that measures upwelling radiances at the top of the atmosphere in the range 270–500 nm (Levelt et al., 2006) since its deployment in 2004. With a 2600 km across track swath and sixty viewing positions, it provided nearly daily global coverage at a 13 × 24 km nadir resolution (28 × 150 at extreme off-nadir) during the first three years of operation. Since mid-2007, an external obstruction to the sensor's field of view, perturbing OMI measurements of both solar flux and Earth shine radiance at all wavelengths, began to progressively develop. Currently, about half the sensor's sixty viewing positions are affected by what is referred to as "row anomaly", since the viewing positions are associated with the row numbers on the CCD detectors. The site http://www.knmi.nl/omi/research/product/rowanomaly-background.php provides details on the onset and progression of the row anomaly.

The OMAERUV algorithm uses as input measured reflectances at 354 and 388 nm to retrieve column atmosphere values of aerosol optical depth (AOD) and single scattering albedo (SSA). Ancillary information on near UV (354 and 388 nm) surface albedo (A_λ), surface type, and aerosol layer height (ALH) is required. Real time AIRS CO measurements are used to identify carbonaceous particles, and ALH is inferred based on CALIOP measurements. The way AIRS CO and CALIOP aerosol height information are

AMTD
6, 5621–5652, 2013

used in the OMAERUV algorithm is the central theme of this paper, and it is discussed at length in Sects. 3 and 4.

2.1 Aerosol models and forward calculations

The algorithm assumes that the atmospheric aerosol column can be represented by one of three aerosol types: desert dust (DD), carbonaceous particles (CB), and sulfate-based (SF) aerosols. Each aerosol type is characterized by a fixed bi-modal spherical particle size distribution (Torres et al., 2007) with parameters derived from long-term AERONET statistics (Dubovik et al., 2002). The relative spectral dependence of the imaginary component of refractive in the 354–388 nm range, Δk, is assumed for each aerosol type (Torres et al., 2007), and recently modified for the CB type to account for the absorption effects of organic carbon (Jethva and Torres, 2011). Each aerosol type is further divided into seven sub-types to account for the variability of the imaginary component of the refractive index at 388 nm, k_{388}, which, in combination with the assumed size distribution, translates into SSA variability.

Forward radiative transfer calculations of upwelling reflectance at the top of the atmosphere (354 and 388 nm) for the resulting 21 aerosol models were used to generate a set of look-up tables (LUT's) with nodal points in viewing geometry, aerosol optical depth (AOD), aerosol single scattering albedo (SSA), and aerosol layer height (ALH).

2.2 Inversion procedure

The measured reflectances are first used to calculate the scene 388 nm Lambert Equivalent Reflectivity (R_{388}), and the absorbing Aerosol Index (AI) as described in Torres et al. (2007). To exclude sub-pixel cloud contamination effects, threshold values of the difference $R_{388} - A_{388}$, (ΔR), are used as upper limits in the allowed aerosol-related reflectivity increases beyond the value of the surface reflectance A_{388}.

Figure 1 shows a schematic overview of OMAERUV's retrieval procedure. At each OMI pixel, the AI, COI (i.e., normalized CO column amount), and surface type (source:

AMTD
6, 5621–5652, 2013

http://www-surf.larc.nasa.gov/surf/pages/data-page.html) are used to select an aerosol type. For simplicity, we define the dimensionless parameter COI (CO index) as the column CO amount (in molecules cm^{-2}) divided by 10^{18} molecules cm^{-2}.

The absorbing aerosol type identification is achieved by examining the values of AI and COI in relation to threshold values, AI_0 and COI_0, that represent respectively AI noise and background COI values not necessarily associated with the free troposphere CO burden which is expected to co-exist with the lofted carbonaceous aerosols. The adopted values of COI_0 are 2.2 and 1.8 for the northern and Southern Hemisphere respectively. The value of AI_0 is 0.8 for both land and ocean conditions. As shown schematically in the upper-left panel of Fig. 1, the presence of carbonaceous aerosols is assumed if $AI \geq AI_0$ and $COI \geq COI_0$, or for $COI > 2.8$ (2.5 in the Southern Hemisphere) regardless of AI considerations. On the other hand, when $AI \geq AI_0$ and $COI < COI_0$ desert dust aerosols are assumed present. If neither set of conditions are met the presence of sulfate aerosols is assumed.

Screening of sub-pixel cloud contamination is carried out making use of AI, ΔR, and the selected aerosol type in an algorithm flagging scheme that assigns confidence levels on the occurrence of cloud-free conditions as shown on the upper right box of Fig. 1. This is done by means of an algorithm Quality Flag (QF) whose value is 0 for minimum cloud presence, and has a value of 1 when it is suspected that the retrieval product is affected by cloud contamination.

Different retrieval approaches are applied over the oceans and the continents. Over the oceans, the retrieval is only carried out when either DD or CB aerosols are present as indicated by the AI parameter. No retrieval takes place over the oceans for AI values less than 0.8. Retrievals over land, on the other hand, are carried out under all conditions regardless of the value of AI. The actual retrieval method depends on the nature of the aerosol signal as indicated by the magnitude of the AI and COI parameters. A two-channel method that allows the simultaneous retrieval of AOD and SSA, or, a single-channel retrieval of AOD is applied depending on aerosol type and AI considerations as shown on the lower right box of Fig. 1. When the single-channel approach

AMTD
6, 5621–5652, 2013

is applied, a SSA of 1.0 is assumed. Retrievals results are obtained for the five ALH nodal point in in the LUT's (surface, 1.5, 3, 6, and 10 km).

A best-guess aerosol layer height must be prescribed as the accuracy of the satellite retrieved properties of absorbing aerosol types in the near UV, is highly sensitive to the aerosol layer altitude above the ground (Torres et al., 1998). The lower left diagram of Fig. 1 describes the steps for ALH determination. For the SF aerosol type, a vertically decaying distribution is used, in which aerosol concentration is largest at the surface and decreases exponentially with height. If either the DD or CB aerosol type has been selected, the best guess ALH is given by a CALIOP-based climatological value (Z_{clp}) developed for this purpose, and discussed in detail in Sect. 4. If the CALIOP climatology does not provide an ALH entry, an ALH assumption is made that depends on aerosol type and location as shown in Fig. 1. Carbonaceous aerosols layers within 30° of the Equator are assumed to have maximum concentration at 3 km above the surface whereas mid and high-latitude (pole wards of ±45°) smoke layers are assumed to peak at 6 km. The height of smoke layers between 30° and 45° latitude in both hemispheres is interpolated with latitude between 3 and 6 km. The location of desert dust aerosol layers varies between 1.5 and 10 km, and is given by a multiyear climatological average of Chemical Model Transport (CTM) calculations using the GOCART model (Ginoux et al., 2001) gridded at a resolution of 2.5°. Thus, in addition to retrievals at five standard ALH values, a retrieval at the best-guess value of ALH is also reported.

3 Combined use of OMI-AI and AIRS-CO for aerosol type identification

In the near-UV, the separation between absorbing and non-absorbing aerosol types is straightforward given the large sensitivity to aerosol absorption in this spectral region. Differentiating between carbonaceous (fine particles) and dust (coarse particles) aerosols in ocean satellite retrieval algorithms that use visible and near IR observations is generally done in terms the well known Angstrom's wavelength exponent (AE) (Angstrom, 1929), whose magnitude is inversely related to the predominant particle

AMTD
6, 5621–5652, 2013

size. Typical AE values vary from nearly zero for high concentrations of desert dust aerosols to values of 2.0 or greater associated with large AOD fine size carbonaceous aerosols (Eck et al., 1999; Toledano et al., 2011). Satellite derived AE for aerosol type differentiation over land is unreliable due to uncertainties associated with surface reflectance characterization (Levy et al., 2010). Because of the short separation of the two channels in the OMAERUV algorithm, the AE concept is not applicable and, therefore, distinguishing between fine and coarse size mode absorbing aerosol types (i.e., carbonaceous versus desert dust aerosols) requires additional external information. Although OMI reflectance measurements up to 500 nm are available their use in AE calculation requires a precise characterization of visible surface albedo currently unavailable.

3.1 Carbonaceous aerosols tracers

Nitrogen dioxide (NO_2) and formaldehyde (HCHO) are important biomass burning byproducts measured by OMI that could be used as carbonaceous aerosol tracers. Because of their relative short lifetimes (only up to a few hours), however, these trace gas are not adequate for tracing the long-range aerosol transport. Carbon monoxide (CO), on the other hand, is the second most abundant trace gas produced by biomass burning (Sinha et al., 2003), and has a multiday-long lifetime that makes it a suitable tracer of long-range transport carbonaceous aerosols. Luo et al. (2010), found a clear spatial correlation between Tropospheric Emission Spectrometer (TES) CO measurements and the OMI Aerosol Index signal of the smoke plume generated by the 2006 Australian fires (Torres et al., 2007; Dirksen et al., 2009). Satellite global daily CO measurements are routinely produced by the Measurements of Pollution in the Troposphere (MOPITT) sensor on the Terra satellite (Pan et al., 1998) and by the Atmospheric Infrared Sounder (AIRS) on the Aqua platform (Aumann et al., 2003). Because of the near-simultaneity of AIRS and OMI observations, the AIRS CO product is used in this analysis.

AMTD
6, 5621–5652, 2013

3.2 The AIRS CO product

The AIRS sensor was deployed on 4 May 2002. It is a cross-track scanning grating spectrometer that measures IR radiation at 2378 channels between 3.7 and 16 µm with a 13.5 km nadir field of view (Aumann et al., 2003). AIRS' CO inversion uses radiances in the 4.50–4.58 µm region. It is considered a robust retrieval because of its strong spectral signature and weak water vapor interference with an estimated accuracy of about 15 % (McMillan et al., 2005). The use of cloud-clearing (Chahine et al., 1974) allows the retrievals of global CO for conditions up to 80 % cloudy (Susskind et al., 2003). In this analysis we used the global daily gridded AIRS column CO product expressed as molecules cm^{-2} at a $1^{\circ} \times 1^{\circ}$ resolution, available at http://daac.gsfc.nasa.gov/AIRS.

3.3 Combined use of CO and AI observations

The spatial distributions of tropospheric CO amounts and atmospheric load of carbonaceous aerosols are naturally correlated as both species are generated by biomass burning. On the other hand, no correlation is expected to exist between tropospheric CO and the atmospheric aerosol burden associated with desert dust particles. An example of the expected relationship between CO and dust and smoke aerosols in shown in Fig. 2. The top panel shows the global spatial distribution of the OMI AI on 7 July 2006. The AI map shows pools of large AI values over Southeastern Canada and Eastern US possibly associated with an advancing smoke layer generated by boreal fires in Canada. Another large absorbing aerosol plume lingers over Equatorial Africa between the Equator and about 10° S, most likely the result of agriculture-related burning practices. Large AI values are also present over the arid areas of Northern Africa, the Arabian Peninsula, and Central Asia, as well as over the Atlantic Ocean indicating the presence of a drifting synoptic scale desert dust plume. The center panel in Fig. 2 shows the AIRS-CO column amount as derived from AIRS observations on the same day. Note that very large values of CO column amounts are observed over the areas dominated by the presence of smoke but not over the large regions occupied by the

AMTD
6, 5621–5652, 2013

desert dust layers. The combined use of the AI and COI (as defined in Sect. 2) parameters allows the separation of smoke/dust plumes as shown on the bottom panel of Fig. 2.

Although this straightforward way of separating absorbing aerosol types works very well in most cases, it may break down under certain circumstances. A notable case when the approach fails, takes place when dust aerosols are present over a region characterized by high CO levels associated with pollution episodes other than smoke. In this case the above described approach will identify the absorbing aerosol type as smoke. This situation is likely to happen over Eastern China during the spring season when the normally high CO levels co-exist with the westerly flow of large amounts of desert dust aerosols from the Gobi and Taklimakan deserts.

The CO-based aerosol type separation technique is particularly useful to pick up the presence of drifting layers of carbonaceous aerosols over arid areas. One such event took place on 27 August 2007 when the smoke plume of the fires in Greece moved south across the Mediterranean reaching Northern Libya and Algeria (Turquety et al., 2009). The aerosol type map in Fig. 3, obtained by the previously described method, shows the unmistakable presence of the Greek fires smoke plume over Northern Africa.

3.4 Boundary layer pollution aerosols

CO measurements are also used in the OMAERUV algorithm to indentify cases of high amounts of carbonaceous aerosols in the boundary layer that would otherwise go undetected by the AI. Large summer AOD values are reported by AERONET observations in rapidly developing industrial regions of the world such as northeastern China and northern India. Because of their low elevation these aerosols yield AI values below the reliability limit (~ 0.8) in the near UV. In addition, because of their extraordinarily large concentrations they were often mistaken as cloud contamination in earlier versions of the algorithm. Correlative analysis of ground-based AOD measurements and satellite CO measurements (not shown) indicate high correlation between the two pa-

AMTD
6, 5621–5652, 2013

rameters. Based on this analysis OMAERUV retrievals are now carried out when the measured COI values are larger than 2.8 (NH) or 2.5 (SH) regardless of the AI value.

4 Combined use of OMI and CALIOP observations

CALIOP is a three-channel lidar on board the CALIPSO platform launched in 28 April 2006 in an ascending polar orbit with a 1.32 p.m. Equator crossing time. It measures polarization insensitive attenuated backscatter at 532 and 1064 nm during both day and night time. In addition, CALIOP measures polarization sensitive backscatter at 532 nm. CALIOP probes the atmosphere between the surface and 40 km a.s.l. at a vertical resolution that varies between 30 and 60 m. The horizontal resolution along the orbital track is 335 m (Winker et al., 2009). CALIOP data is available since mid-June 2006 and, except for minor interruptions, continues to be available to present. In addition to the attenuated backscatter profile data, CALIOP's aerosol products includes a Vertical Feature Mask that characterizes particle layers as either cloud or any of several aerosol types, and an aerosol optical depth product. In this study we use daytime observations of the 1064 nm attenuated backscatter. Unlike AIRS global daily coverage, CALIOP's narrow 335 m footprint does not allow the direct use of daily observations as no global coverage is available. Therefore, developing a climatological data set is the best way to make use of CALIOP provided aerosol layer height data.

4.1 Collocation

The OMI sensor makes observations at sixty positions (or viewing angles) across the orbital track. Positions 30 and 31 are closest to nadir. At launch, CALIPSO's subsatellite point coincided with OMI's scan position 45 on the right side of the OMI scan for most of the orbit at low and mid-latitudes, and the time difference between OMI and CALIOP daytime observations was about 13 min. As the Aura satellite orbit was changed to reduce the overpass time difference with that of Aqua, the OMI

AMTD
6, 5621–5652, 2013

scan position of coincidence with CALIOP's observations changed to 37 over several months, and by the end of the orbital maneuver the time observation difference between CALIOP and OMI decreased to about 7 min.

At the 335 m CALIOP's horizontal resolution, there are 39 CALIOP profiles of attenuated backscatter per OMI-CALIOP collocation pixel (OCCP) along CALIPSO's orbital track. In this work we use a specially created set of orbital files that contain merged OMI and CALIOP data collocated along CALIPSO's orbital track. The OMI level 2 data subset coincident with CALIOP's measurements was produced by the A-Train Data Depot (ATDD) project at the Goddard Earth Sciences Data and Information Services Center to address the differences in spatial, vertical, and horizontal, as well as temporal scales of coverage of different instruments participating in the A-Train (Savtchenko et al., 2008). The ATDD data set was augmented with CALIOP's observations of attenuated backscatter at 532 and 1064 nm. In addition to the CALIOP backscatter data and ancillary information, the merged orbital files contain OMI measured radiances, viewing geometry, ancillary data and original retrieval results at the OCCP plus four additional OMI pixels on each side of the OCCP for a total of 9 pixels.

4.2 Cloud screening

The available CALIOP backscatter profiles per OCCP were combined to create an average profile representative of the vertical distribution of the atmospheric load of carbonaceous and/or desert dust aerosols over the OCCP. An attempt to minimize the effect of cloud contamination on both observations was carried out by applying cloud screening procedures to both OMI and CALIOP observations as described by Chen et al. (2012). Heavily cloud contaminated OMI data was excluded by rejecting observations where the OCCP derived Lambert Equivalent Reflectivity (LER) was larger than 25 %. The calculated average CALIOP profiles were screened for the presence of clouds by excluding those layers where the resulting average backscatter was larger than 0.005. The effect of noise was also excluded by rejecting layers where average backscatter was smaller than 0.0015. Figure 4 shows CALIOP's average attenuated backscatter

AMTD
6, 5621–5652, 2013

profiles associated with a carbonaceous aerosol layer in South America (left panel), and a desert dust layer in Northern Africa (right panel) calculated using both 532 and 1064 nm CALIOP observations. While no apparent difference in sensitivity between the 532 and 1064 channels is observed for desert dust particles (right panel), it appears that in the presence of biomass burning aerosols (left panel) the 532 nm measurement losses sensitivity to aerosols near the surface If low level aerosols are not accounted for, the derived aerosol layer altitude would be biased high. For that reason, in this analysis we use CALIOP's 1064 nm measurements that are sensitive to the presence of carbonaceous and desert dust aerosols all the way to the surface.

4.3 Aerosol layer height calculation

In reducing the CALIOP measured profiles, it was assumed that the vertical structure of the tropospheric aerosol load can be represented as a single layer of height ALH. This assumption seeks to facilitate the use of the resulting climatology as input to global retrieval algorithms. Although, multiple aerosol layers are common, elevated dust or carbonaceous particles are most frequently observed as single layers. The parameter Z_{aer} was calculated as the attenuated-backscatter-weighted height according to the expression

$$Z_{\text{aer}} = \sum_{i-1}^{n} H(i) \left[\frac{B_{\text{sc}}(i)}{\sum_{i=1}^{n} B_{\text{sc}}(i)} \right], \quad (1)$$

where $B_{\text{sc}}(i)$, is the attenuated backscatter at height $H(i)$, and n is the number of layers between the surface and 10 km. The resulting aerosol layer height was assumed to be representative of the aerosol layer altitude at the OCCP. The information on aerosol layer height at the fine CALIOP resolution was propagated a few hundred meters beyond the OCCP. The aerosol layer height at the OCCP was also assumed to be representative of the aerosol altitude at any pixel in the nine-OMI-pixel subset (i.e., within

AMTD
6, 5621–5652, 2013

approximately 100 km of the OCCP in the same swath) if the presence of dust or smoke was detected according to the AI. By the same token, if for an OCCP pixel the CALIOP height was undetermined (due to excessive cloud contamination) but the AI on other non-OCCP pixels in the same swath indicated aerosol presence the height for the corresponding pixel-position from the previous across- track-scan was assumed if available. It should be emphasized that the resulting aerosol height data set is not a general representation of the altitude of all aerosol types but it is specifically designed to account for the height of elevated carbonaceous and desert dust aerosol layers when present.

Figure 5 shows three examples of the resulting aerosol layer height derived from 1064 nm CALIOP measurements as previously described. The solid line indicates the effective aerosol layer height calculated using Eq. (1), and the dashed line represents the aerosol layer height assumed in the previous version of OMAERUV algorithm (Torres et al., 2007). CALIOP's observed vertical structure of the aerosol load on 4 April 2007 near the Bodele depression in the Central Saharan desert shows the unmistakable signature of a rising column of dust between the surface and about 3 km at 16° N, 12° E is shown on the top panel of Fig. 5. The airborne dust plume spreads north and south of the source in an atmospheric layer between 3 and 5 km. The aerosol layer height assumed in the OMAERUV algorithm is underestimated by as much as 2 km in relation to that inferred from CALIOP observations.

The center panel illustrates the vertical structure of a smoke layer as seen by the CALIPSO lidar on 12 August 2006 over Angola and Namibia, and the Southern Atlantic Ocean. CALIOP observations show the westward flow of smoke from fires in Angola and Namibia over the Southern Atlantic Ocean. The CALIOP curtain image shows a south-north transect of the smoke layer along the western coast of Central Africa from Angola, covering Angola's coastal waters (~ 12° S, 13° E), and reaching land again over the republic of Congo's coastal area (~ 5° S, 11.5° E). Over the central and northern sections of the transect, the aerosol layer is clearly located above low clouds. The smoke layer over land generated from fires in Angola and Namibia occupies a 2.5 km

AMTD
6, 5621–5652, 2013

thick layer that goes from the surface (about 1 km a.s.l.) to 3.5 km as indicated by the attenuated backscatter signal. The assumed aerosol layer height is consistently higher than the CALIOP derived value.

A layer of carbonaceous aerosols as seen by the OMI and CALIOP sensors over Central Brazil on 30 September 2007 is depicted on the bottom panel of Fig. 5. The CALIOP curtain plot depicts the vertical structure of the layer over a region between 10° S and 30° S along CALIOPS's orbital track. On the northern most end of the plume, the aerosol load is located in a 1 km thick layer between 3 and 4 km above the ground, and widens towards the south. In general, the assumed height is about 1 km higher than the CALIOP-based estimate.

4.4 CALIOP-based aerosol height climatology

The procedure described in the previous section to derive an effective aerosol layer height was applied to the global CALIOP record over the two year period from July 2006 to December 2008. The extension beyond 2008 was hindered by the loss of the OCCP resulting from the onset of the OMI row anomaly discussed in Sect. 2. Gridded $1^\circ \times 1^\circ$ resolution monthly averages of ALH were calculated. A minimum of five data points per-grid were required to produce a monthly value. Extracts from a degraded $5^\circ \times 5^\circ$ gridded product was used to fill gaps in the original $1^\circ \times 1^\circ$ product resulting from CALIOP's lack of global coverage and the interference of clouds. Additionally, image processing techniques using convolution and Gaussian smoothing (Gonzalez and Woods, 1992) were applied to reduce the noise and minimize the effect of isolated maxima and minima.

Figure 6 shows global maps of the monthly averaged aerosol layer height (Z_{clp}), in km above surface, derived from CALIOP observations. Maps shown correspond to the mid-season months (January, April, July, October).

The Z_{clp} spatial distribution in January is dominated by the presence of desert dust and carbonaceous aerosols copiously produced by their emission sources in the Saharan (desert dust) and Equatorial Africa (biomass burning). Z_{clp}'s between 3 and 4 km

AMTD
6, 5621–5652, 2013

predominate over the Northern African deserts, while values between 2 and 3 km are observed associated with the fire activity in the tropical belt along the Atlantic coast from Guinea to Nigeria, and extending eastwards to Ethiopia. Over the northern Atlantic Ocean, Z_{clp} descends rapidly westwards from over 2 km at the Northern African West coast to the 45° W meridian, and continues to decrease, with some oscillations, to minimum values of about 1 km over the Gulf of Mexico. Z_{clp}'s around 3 km can be observed over the SE United States as a consequence of local fires, as well as long range transport from Central America. High Z_{clp} values are also observed in the Southern Hemisphere Summer over the land masses of South America (Patagonia), Western Africa, and Australia where desert dust production and smoke from brush fires (Australia) are commonly observed in January.

A significant narrowing in the Z_{clp} north-south distribution over the Atlantic Ocean is apparent in Spring following the conclusion of the Equatorial Africa biomass burning season. Z_{clp} values higher than those observed in winter are apparent over the Atlantic Ocean owing to the Spring activation of Saharan dust sources. Elevated layers (3 km and higher) can be observed over the eastern half of the continental US, generally resulting from the transport of carbonaceous aerosols from boreal wild fires in Canada (northeast) and local sources, as well as contribution from transport from Mexico and Central America (southeast). The observed Z_{clp}'s lower than 3 km over the western half of the US are likely associated with local dust production. As a consequence of the activation of dust sources in Central Asia, elevated layers (3 km and higher) are apparent over Afghanistan, Turkmenistan, and Uzbekistan. Long range transport of desert dust from the Saharan sources across the Mediterranean, and from sources in Central Asia trigger the spread of dust aerosol layers about 2.5 km high over western and northern Europe. Eastward transport of desert dust following the Spring activation of the Gobi and Taklamakan deserts, and layers of carbonaceous aerosols from biomass burning in Southeast Asia linger over East Asia in layers 2 to 3 km high.

An enhanced Summer Z_{clp}, associated with the northward spread of aerosol layers from boreal fires in Canada and Siberia, is observed at about 3 km. The Summer

AMTD
6, 5621–5652, 2013

Saharan aerosol layer over the Atlantic Ocean between 10° N and 30° N varies in altitude between 3.5–40 km at the West Coast of Northern Africa going down towards the West, reaching 1.5 km over the Gulf of Mexico. Smoke from biomass burning activity in Central Africa spills over the Southern Atlantic Ocean in an aerosol layer at 2–2.5 km.

The Autumn global aerosol height distribution is characterized by an overall Z_{clp} decrease. Except for a height increase over the biomass burning regions in the Southern Hemisphere, Autumn Z_{clp} values are lower than the previous season values by 1–2 km over most of the globe. The Saharan Layer Z_{clp} over the Atlantic Ocean reaches values as low as 1.5 km about halfway between Northern Africa and the Gulf of Mexico. The carbonaceous aerosol layer, known as the "river of smoke", flowing off Southeast Africa along the Indian Ocean at a 1 ∼ 2 km height Z_{clp} is clearly observed.

5 Evaluation of improvements in OMAERUV retrievals

A brief discussion of the effect of the algorithm upgrades on retrieved products is presented here. Comprehensive assessments of the OMAERUV products using ground based and other satellite observations are discussed in detail by Ahn et al. (2013) and Jethva et al. (2013).

The effect of using the CALIOP Z_{clp} climatology as input in the OMI inversion algorithm, was evaluated by comparing the optical depth from the OMAERUV algorithm to AERONET observations using both the standard algorithm aerosol height assumption and the aerosol altitude extracted from the CALIOP climatology described here. The assessment exercise was carried out using AERONET measurements at the five sites listed in Table 1, where the presence of elevated dust and smoke layers is routinely observed. Columns 4 through 8 in Table 1 show respectively the resulting correlation coefficient (r), intercept, the rms, and the number of retrievals within 10 % (Q_{10}) and 30 % (Q_{30}) of the AERONET values, for both the standard aerosol layer height assumption, and the CALIOP provided height information. The standard OMAERUV method of prescribing aerosol layer height of desert dust layers based on a model-generated climatol-

AMTD
6, 5621–5652, 2013

ogy works fairly well as indicated the correlation coefficients between 0.71 and 0.83 at the five locations. Small but important improvement in these statistics is obtained when the CALIOP-based climatology of aerosol layer height. The CALIOP-based approach yields higher correlation coefficients (between 0.74 and 0.84) and slightly smaller intercepts. The improvement is noticeable in terms of the Q_{10} and Q_{30} parameters, defined as the number of points (in percent) within 10 % and 30 % of the ground truth observations. Q_{10} went up between 3 and 17 % at the five sites whereas Q_{30} increased between 3 % and 11 %. In most cases the effect of using the CALIOP-based aerosol layer height was to reduce AERONET-OMI differences in the winter season when the aerosol layer height is under-estimated by the standard assumption. The observed improvement is smallest in the middle of the Saharan Desert (Tamanrasset site) and increases rapidly away from the dust aerosol source areas with the largest improvement registered at Dakar. The scatter plot in Fig. 7 illustrates the resulting OMAERUV AOD improvement in relation to AERONET observations at the Banizoumbou AERONET site.

As illustrated in Fig. 3, the use of CO measurements as an aerosol tracer has facilitated the identification of carbonaceous aerosols over arid regions, where the distinction between dust and smoke particles would not have been possible without the availability of CO observations. The AIRS CO data has also enabled the detectability and characterization of high levels of boundary layer pollution aerosols undetectable by the previous OMAERUV algorithm without the help of AIRS CO data. Figure 8 depicts the retrieved fields of aerosol optical and single scattering albedo on 20 August 2007 over Northeastern China by the previous (top) and current (bottom) versions of the algorithm.

6 Summary and conclusions

We have documented the use of CALIOP aerosol vertical distribution information and AIRS CO column amounts to provide information on aerosol layer height and aerosol type necessary for the retrieval of AOD and SSA by the OMAERUV algorithm. The

AMTD
6, 5621–5652, 2013

combined use in real time of observations from sensors on two different satellites is only possible thanks to the near-simultaneity of A-train observations.

It has been shown that the combined use of AIRS CO observations and the OMI UV aerosol index provides a way of reliably identifying the absorbing aerosol type when absorbing aerosols have been positively detected via the AI. Because CO is an adequate tracer of carbonaceous aerosols, elevated values of both AI and CO correspond in most cases to the presence of smoke layers whereas the occurrence of high AI values and low CO amounts is associated with layers of desert dust aerosols. Another useful application of the AIRS CO data is the identification of high boundary layer aerosol loads that would otherwise be dismissed as cloud contamination by OMAERUV. Because of the large aerosol load associated with these events over biomass burning regions and Eastern China, it is possible to retrieve both aerosol optical depth and single scattering albedo.

We made use of time and space collocated CALIOP and OMI observations for the determination of the height of elevated layers of carbonaceous and desert dust aerosols detected by OMI's near UV observations. An effective aerosol layer height was calculated as the attenuated-backscatter-weighted average height obtained from CALIOP's 1064 nm measurements. Observations at 1064 nm were chosen over the 532 nm measurements because of apparent saturation effects at the shorter wavelength. The OMI-CALIOP combined analysis was carried out over a 30 month record from July 2006 to December 2008, when instrumental issues affecting the OMI sensor resulted in the loss of the collocation capability.

A 30 month climatology of aerosol layer height was calculated. The impact of using CALIOP-based climatology of aerosol layer height was evaluated by comparing OMI retrieved AOD's to AERONET observations at a number of locations in Northern Africa. Validation results indicate that although previous algorithm assumptions on aerosol layer height worked reasonably well, the use of the CALIOP-based climatology produces a noticeable improvement of retrieval results. The CALIOP-based absorbing

AMTD
6, 5621–5652, 2013

aerosol layer height climatology and the real-time use of AIRS CO observations have been integrated into the current version of the OMAERUV algorithm.

References

Ahn, C., Torres, O., and Bhartia, P. K.: Comparison of OMI UV aerosol products with Aqua-MODIS and MISR observations in 2006, J. Geophys. Res, 113, D16S27, doi:10.1029/2007JD008832, 2008.

Ahn, C., Torres, O., and Jethva, H.: Assessment of OMI near UV aerosol products, Part 1: Evaluation of aerosol optical depth, J. Geophys. Res., in review, 2013.

Anderson, T. L., Charlson, R. J., Bellouin, N., Boucher, O., Chin, M., Christopher, S. A., Haywood, J., Kaufman, Y. J., Kinne, S., Ogren, J. A., Remer, L. A., Takemura, T., Tanre, D., Torres, O., C. R. Trepte, Wielicki, B. A., Winker, D. M., and Yu, H.: An "A-Train" strategy for quantifying direct climate forcing by anthropogenic aerosols, B. Am. Meteorol. Soc., 86, 1795–1809, 2005.

Angstrom, A.: On the atmospheric transmission of Sun radiation and on dust in the air, Geogr. Ann., 12, 130–159, 1929.

Aumann, H. H., Chahine, M. T., Gautier, C., Goldberg, M. D., Kalnay, E., McMillin, L. M., Rivercomb, H., Rosenkranz, P. W., Smith, W. L., Staelin, D. H., Strow, L. L., and Susskind, J.: AIRS/AMSU/HSB on the aqua mission: design, science objectives, data products, and processing systems, IEEE Trans. Geosci. Remote Sens., 41, 253–264, 2003.

Chahine, M. T.: Remote sounding of cloudy atmospheres, I, The single cloud layer, J. Atmos. Sci., 31, 233– 243, 1974.

Chen, Z., Torres, O., McCormick, M. P., Smith, W., and Ahn, C.: Comparative Study of aerosol and cloud detected by CALIPSO and OMI, Atmos. Environ., 51, 187–195, 2012.

De Graaf, M. and Stammes, P.: SCIAMACHY Absorbing Aerosol Index – calibration issues and global results from 2002–2004, Atmos. Chem. Phys., 5, 2385–2394, doi:10.5194/acp-5-2385-2005, 2005.

De Graaf, M., Stammes, P., Torres, O., and Koelemeijer, R. B. A.: Absorbing aerosol index: sensitivity analysis, application to GOME and comparison with TOMS, J. Geophys. Res., 110, D01201, doi:10.1029/2004JD005178, 2005.

AMTD
6, 5621–5652, 2013

Dirksen, R. J., Folkert Boersma, K., de Laat, J., Stammes, P., van der Werf, G. R., Val Martin, M., and Kelder, H. M.: An aerosol boomerang: rapid around-the-world transport of smoke from the December 2006 Australian forest fires observed from space, J. Geophys. Res., 114, D21201, doi:10.1029/2009JD012360, 2009.

Dubovik, O., Holben, B., Eck, T. F., Smirnov, A., Kaufman, Y. J., King, M. D., Tanre, D., and Slutsker, I.: Variability of absorption and optical properties of key aerosol types observed in worldwide locations, J. Atmos. Sci., 59, 590–608, 2002.

Eck, T. F., Holben, B. N., Reid, J. S., Dubovik, O., Smirnov, A., O'Neill, N. T., Slutsker, I., and Kinne, S.: Wavelength dependence of the optical depth of biomass burning, urban and desert dust aerosols, J. Geophys. Res., 104, 31333–31349, 1999.

Ginoux, P., Chin, M., Tegen, I., Prospero, J. M., Holben, B., Dubovik, O., and Lin, S.-J.: Sources and distributions of dust aerosols simulated with the GOCART model, J. Geophys. Res., 106, 20255–20273, doi:10.1029/2000JD000053, 2001.

Gleason, J., Hsu, N. C., and Torres, O.: Biomass burning smoke measured using backscattered ultraviolet radiation: SCAR-B and Brazilian smoke inter annual variability, J. Geophys Res., 103, 31969–31978, 1998.

Gonzalez, R. and Woods, R.: Digital Image Processing, Addison-Wesley Publishing Company, Reading, MA, 191 pp., 1992.

Herman, J. R., Bhartia, P. K., Torres, O., Hsu, C., Seftor, C., and Celarier, E.: Global Distribution of UV-absorbing aerosols from Nimbus-7/TOMS data, J. Geophys. Res., 102, 16911–16922, 1997.

Hsu, N. C., Herman, J. R., Bhartia, P. K., Seftor, C. J., Thompson, A. M., Gleason, J. F., Eck, T. F., and Holben, B. N.: Detection of biomass burning smoke from TOMS measurements, Geophys. Res. Lett., 23, 745–748, 1996.

Jethva, H. and Torres, O.: Satellite-based evidence of wavelength-dependent aerosol absorption in biomass burning smoke inferred from Ozone Monitoring Instrument, Atmos. Chem. Phys., 11, 10541–10551, doi:10.5194/acp-11-10541-2011, 2011.

Jethva, H., Torres, O., and Ahn, C.: Assessment of OMI near UV aerosol products, Part 2: Comparison of single scattering Albedo to ground-based AERONET observations in biomass burning and dust environments, J. Geophys. Res., in review, 2013.

Levelt, P. F., Hilsenrath, E., Leppelmeier, G. W., van den Ooord, G. H. J., Bhartia, P. K., Tamminen, J., de Haan, J. F., and Veefkind, J. P.: Science objectives of the Ozone Monitoring Instrument, IEEE Trans. Geosci. Remote Sens., 44, 1093–1101, 2006.

AMTD
6, 5621–5652, 2013

Levy, R. C., Remer, L. A., Kleidman, R. G., Mattoo, S., Ichoku, C., Kahn, R., and Eck, T. F.: Global evaluation of the Collection 5 MODIS dark-target aerosol products over land, Atmos. Chem. Phys., 10, 10399–10420, doi:10.5194/acp-10-10399-2010, 2010.

Luo, M., Boxe, C., Jiang, J., Nassar, R., and Livesey, N.: Interpretation of Aura satellite observations of CO and aerosol index related to the December 2006 Australia fires, Remote Sens. Environ., 114, 2853–2862, 2010.

McMillan, W. W., Barnet, C., Strow, L., Chahine, M. T., McCourt, M. L., Warner, J. X., Novelli, P. C., Korontzi, S., E. S. Maddy, and Datta, S.: Daily global maps of carbon monoxide from NASA's atmospheric infrared sounder, Geophys. Res. Lett., 32, L11801, doi:10.1029/2004GL021821, 2005.

Pan, L., Guille, J. C., Edwards, D. P., and Bailey, P. L.: Retrieval of tropospheric carbon monoxide for the MOPITT experiment, J. Geophys. Res., 103, 32277–32290, 1998.

Penning de Vries, M. J. M., Beirle, S., and Wagner, T.: UV Aerosol Indices from SCIAMACHY: introducing the SCattering Index (SCI), Atmos. Chem. Phys., 9, 9555–9567, doi:10.5194/acp-9-9555-2009, 2009.

Savtchenko, A., Kummerer, R., Smith, P., Gopalan, A., Kempler, S., and Leptoukh, G.: A-Train data depot: bringing atmospheric measurements together, IEEE Trans. Geos. Rem. Sens., 46, 2788–2795, 2008.

Seftor, C. J., Hsu, N. C., Herman, J. R., Bhartia, P. K., Torres, O., Rose, W. I., Schneider, D. J., and Krotkov, N.: Detection of volcanic ash clouds from Nimbus7/total ozone mapping spectrometer, J. Geophys. Res., 102, 16749–16759, 1997.

Sinha, P., Hobbs, P. V., Yokelson, R. J., Bertschi, I. T., Blake, D. R., Simpson, I. J., Gao, S., Kirchstetter, T. W., and Novakov, T.: Emissions of trace gases and particles from savanna fires in southern Africa, J. Geophys. Res., 108, 8487, doi:10.1029/2002JD002325, 2003.

Susskind, J., Barnet, C. D., and Blaisdell, J. M.: Retrieval of atmospheric and surface parameters from AIRS/AMSU/HSB data in the presence of clouds, IEEE Trans. Geosci. Remote Sens., 41, 390–409, 2003.

Swap, R. J., Annegarn, H. J., Suttles, J. T., King, M. D., Platnick, S., Privette, J. L., and Scholes, R. J.: Africa burning: a thematic analysis of the Southern African Regional Science Initiative (SAFARI 2000), J. Geophys. Res., 108, 8465, doi:10.1029/2003JD003747, 2003.

Toledano, C., Wiegner, M., Groß, S., Freudenthaler, V., Gasteiger, J., Muller, D., Schladitz, A., Weinzierl, B., Torres, B., and O'Neill, N. T.: Optical properties of aerosol mixtures from sun-sky radiometry during SAMUM-2, Tellus B, 63, 635–648, 2011.

AMTD
6, 5621–5652, 2013

Torres, O., Bhartia, P. K., Herman, J. R., and Ahmad, Z.: Derivation of aerosol properties from satellite measurements of backscattered ultraviolet radiation, theoretical basis, J. Geophys. Res., 103, 17099–17110, 1998.

Torres, O., Bhartia, P. K., Herman, J. R., Syniuk, A., Ginoux, P., and Holben, B.: A long term record of aerosol optical depth from TOMS observations and comparison to AERONET measurements, J. Atmos. Sci., 59, 398–413, 2002.

Torres, O., Tanskanen, A., Veihelman, B., Ahn, C., Braak, R., Bhartia, P. K., Veefkind, P., and Levelt, P.: Aerosols and surface UV products from OMI Observations: an overview, J. Geophys. Res., 112, D24S47, doi:10.1029/2007JD008809, 2007.

Turquety, S., Hurtmans, D., Hadji-Lazaro, J., Coheur, P.-F., Clerbaux, C., Josset, D., and Tsamalis, C.: Tracking the emission and transport of pollution from wildfires using the IASI CO retrievals: analysis of the summer 2007 Greek fires, Atmos. Chem. Phys., 9, 4897–4913, doi:10.5194/acp-9-4897-2009, 2009.

Winker, D. M., Pelon, J., and McCormick, M. P.: "The CALIPSO mission: Spaceborne lidar for observation of aerosols and clouds", Proc. SPIE, 4893, 1–11, 2003.

AMTD
6, 5621–5652, 2013

Table 1. Evaluation of improved aerosol layer height characterization.

AERONET	Location		Number	r		Intercept		RMS		Q_{10}		Q_{30}	
Site	Lat.	Lon.	points	Std.	Cal	Std.	Cal	Std.	Cal	Std.	Cal	Std.	Cal
Agoufou	22.8° N	5.5° E	184	0.82	0.83	0.13	0.10	0.17	0.16	50	58	64	71
Tamanrasset	15.3° N	1.5° E	98	0.83	0.84	0.09	0.08	0.10	0.10	60	63	66	69
Banizombou	13.5° N	2.7° E	182	0.71	0.75	0.21	0.17	0.19	0.16	45	53	57	67
Dakar	14.4° N	17.0° W	163	0.73	0.74	0.14	0.12	0.19	0.15	39	56	58	69
IER_Cinzana	13.3° N	5.9° W	118	0.79	0.83	0.09	0.08	0.21	0.17	35	47	50	60

AMTD
6, 5621–5652, 2013

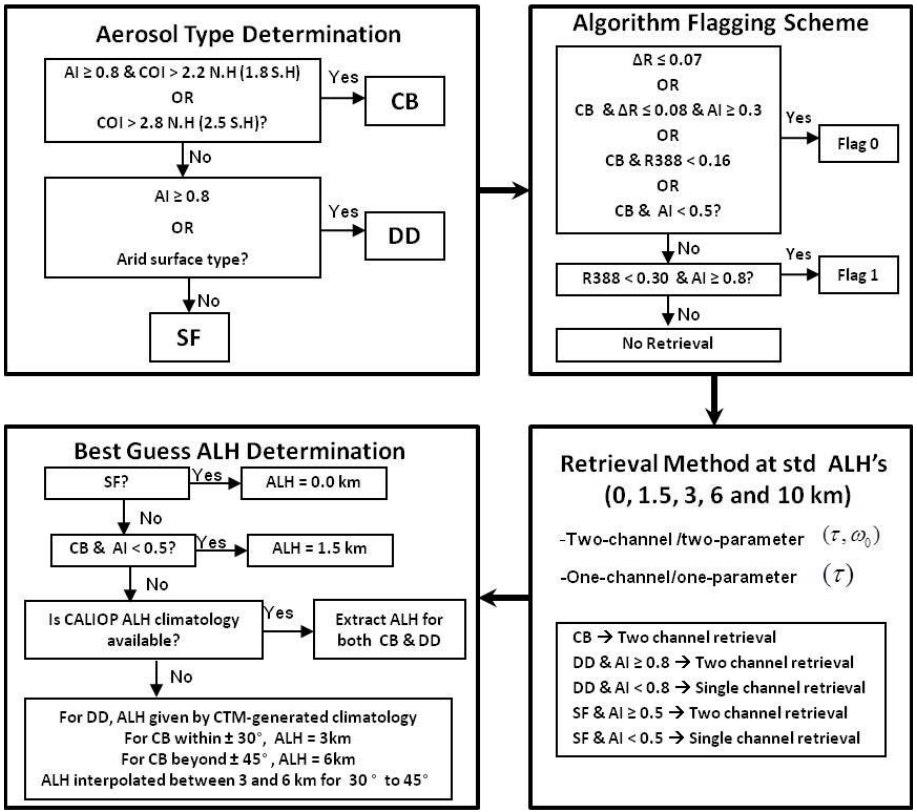

Fig. 1. Graphic description of OMAERUV inversion scheme.

AMTD
6, 5621–5652, 2013

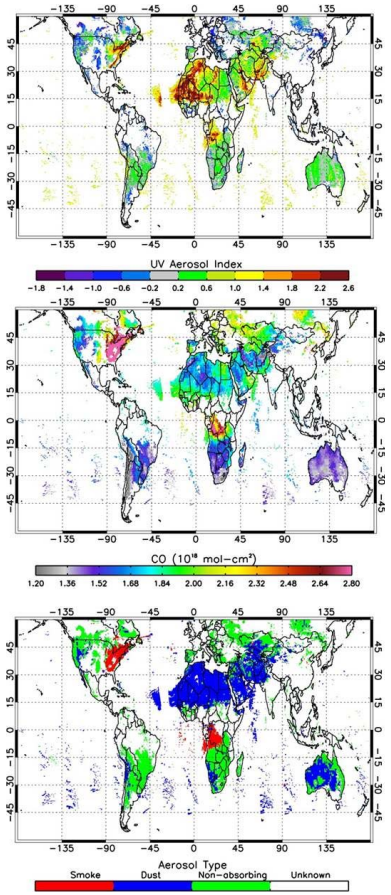

Fig. 2. OMAERUV Aerosol Index on 7 July 2006 **(a)**, AIRS CO amounts **(b)**, **(c)** aerosol type classification.

AMTD
6, 5621–5652, 2013

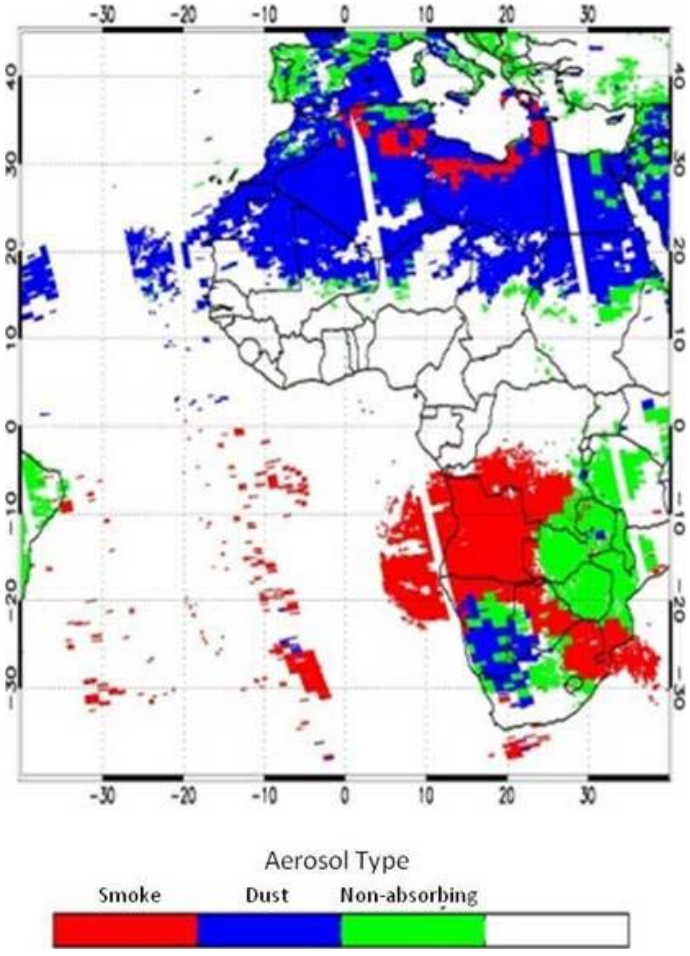

Fig. 3. Aerosol type over Africa on 27 August 2007 (see text for details).

AMTD
6, 5621–5652, 2013

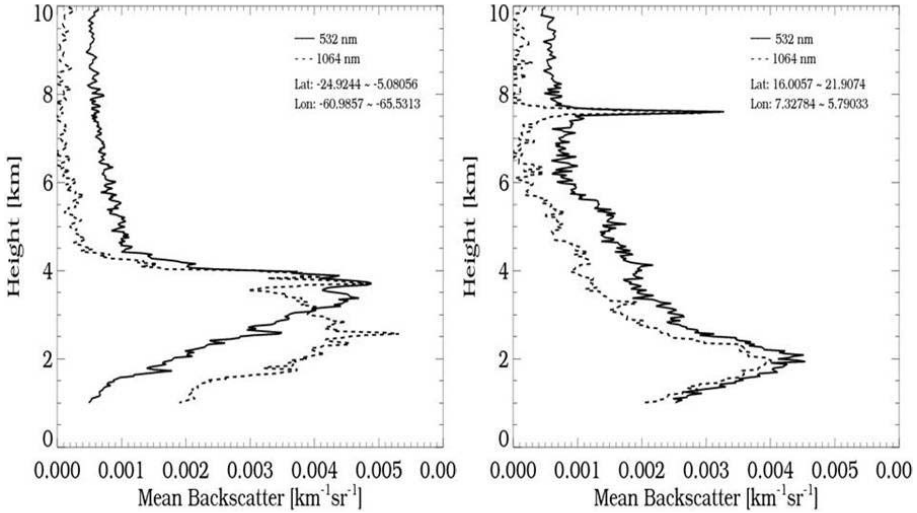

Fig. 4. CALIOP-measured attenuated backscatter profiles at 532 nm (solid line) at 1064 nm (dotted line) over Amazonia (left) and Saharan Desert (right).

AMTD
6, 5621–5652, 2013

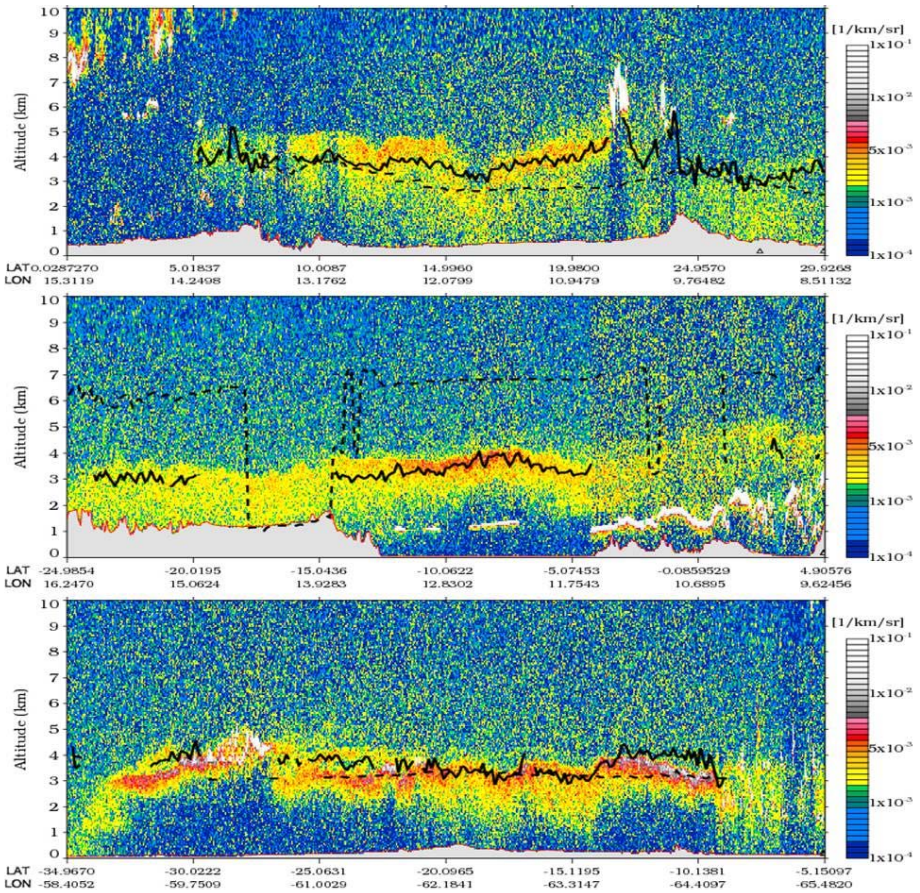

Fig. 5. Sample derived aerosol layer height and CALIOP-measured 1064 nm backscatter for three aerosol episodes: top: top; middle, middle; bottom: bottom.

AMTD
6, 5621–5652, 2013

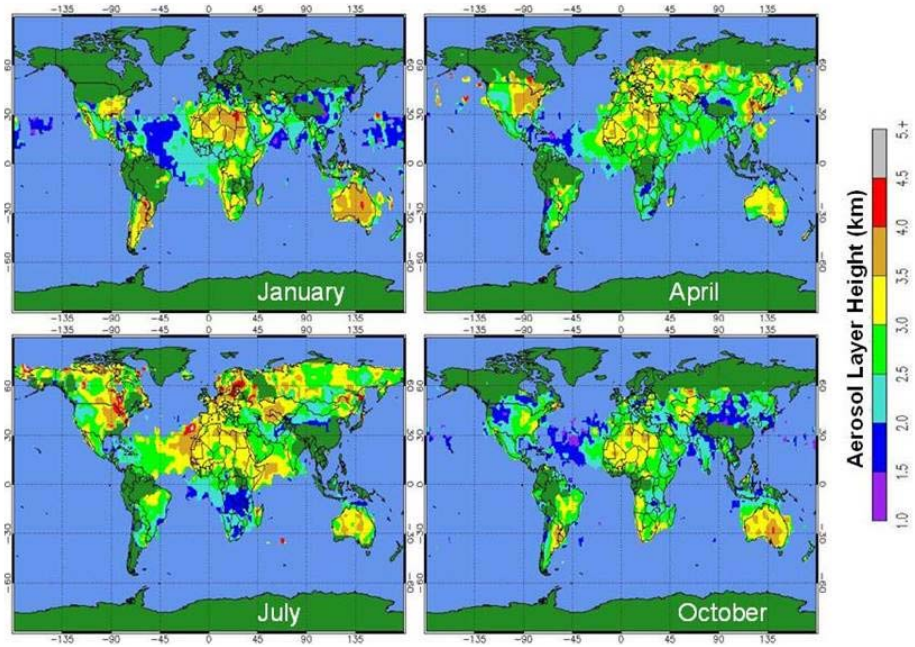

Fig. 6. Monthly average aerosol layer height.

AMTD
6, 5621–5652, 2013

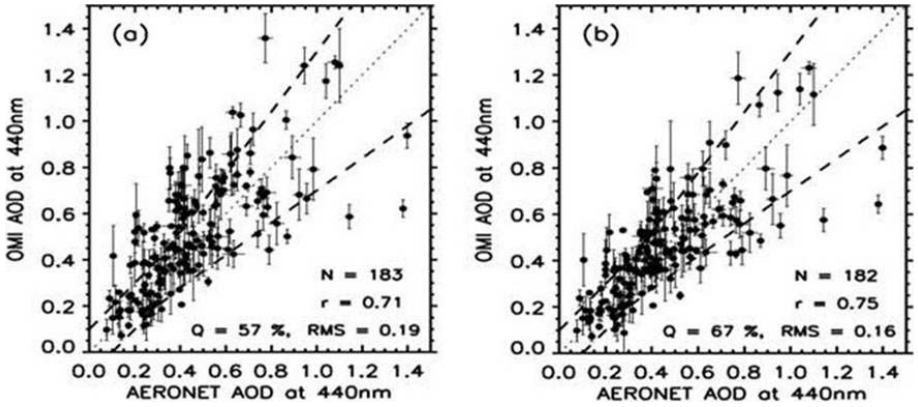

Fig. 7. Evaluation of AOD retrieval using standard aerosol layer height assumption (left) and CALIOP climatology (right) at the Banizoumbou site.

AMTD
6, 5621–5652, 2013

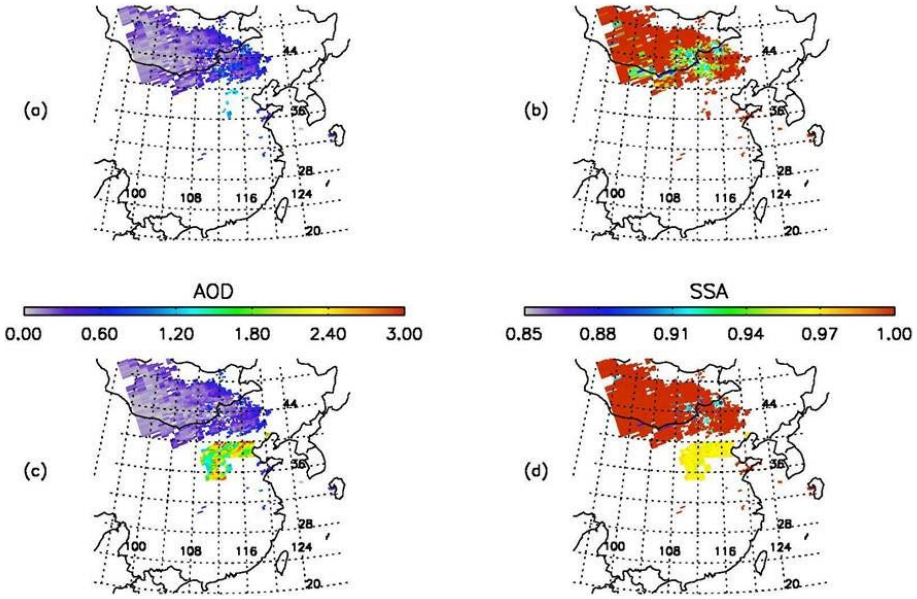

Fig. 8. Retrieved AOD and SSA at 388 nm from the previous **(a, b)** and improved **(c, d)** OMI UV algorithm over Northeastern China on 20 August 2007.

AMTD
6, 5621–5652, 2013